Supporting Material

Vibrational Dynamics of Icosahedrally Symmetric Biomolecular Assemblies Compared with Predictions Based on Continuum Elasticity

Zheng Yang, Ivet Bahar, and Michael Widom

Supplementary material for "Vibrational Dynamics of Icosahedrally Symmetric Biomolecular Assemblies Compared with Predictions Based on Continuum Elasticity"

by Zheng Yang, Ivet Bahar and Michael Widom

Appendix A: Spherical harmonics
Appendix B: Bondary conditions
Appendix C: Mackay icosahedron and toy models
Appendix D: Satellite Tobacco Mosaic Virus (full capsid)
Appendix E: Brome Mosaic Virus

APPENDIX A: Spherical harmonics

Spherical harmonics and vector spherical harmonics, respectively, comprise complete basis sets for scalar and and vector fields on the sphere. Consider a scalar field $\rho(\theta, \phi)$. Completeness assures us we can write

$$\rho(\theta, \phi) = \sum_{l,m} \rho_{lm} Y_{lm}, \tag{A-1}$$

and we can use orthogonality of the spherical harmonics to obtain the expansion coefficients

$$\rho_{lm} = \int Y_{lm}^{\star}(\theta, \phi) \rho(\theta, \phi) d\Omega \tag{A-2}$$

where $d\Omega = \sin\theta d\theta d\phi$ ranges over 4π of solid angle. Similarly, an arbitrary vector field $\mathbf{u}(\theta, \phi)$ can be expressed in terms of vector spherical harmonics (1) as

$$\mathbf{u}(\theta, \phi) = \sum_{l,m} [A_{lm} \mathbf{V}_{lm}(\theta, \phi) + B_{lm} \mathbf{W}_{lm}(\theta, \phi) + C_{lm} \mathbf{X}_{lm}(\theta, \phi)] \tag{A-3}$$

and the expansion coefficients can be obtained through

$$A_{lm} = \int \mathbf{V}_{lm}^{\star}(\theta, \phi) \cdot \mathbf{u}(\theta, \phi) d\Omega \tag{A-4}$$

and analogous equations for B_{lm} and C_{lm}.

Projection onto spherical harmonics provides a simple way to classify the symmetry of scalar functions. If $\rho(\theta, \phi)$ has spherical symmetry (i.e., is a constant, independent of θ

1

and ϕ) then its projection onto Y_{lm} vanishes except for $l = m = 0$. If instead $\rho(\theta, \phi)$ has icosahedral symmetry (i.e., is not constant but is invariant under rotations belonging the the icosahedral symmetry group) then its projection onto Y_{lm} vanishes except for $l = 0, 6, 10, 12, ...$ (2). If $\rho(\theta, \phi)$ has nonvanishing projections onto other values of l then it has symmetry lower than icosahedral.

For a given l the coefficients ρ_{lm} depend on the choice of spatial coordinates. We can form a rotationally invariant measure of the angular momentum projections as

$$\rho_l = \left[\frac{4\pi}{2l+1} \sum_{m=-l}^{l} |\rho_{lm}|^2 \right]^{1/2}. \tag{A-5}$$

Then ρ_6/ρ_0 measures the reduction of spherical symmetry to icosahedral, and the ratio of ρ_l/ρ_6 measures the degree to which icosahedral symmetry is broken. For example, nonzero ρ_4 indicates tetrahedral or cubic symmetry breaking.

Alternatively, we can express icosahedrally symmetric functions of spatial position as a superposition of "icosahedral harmonics" (3). The simplest icosahedral harmonic I_0 is just a constant. The next icosahedral harmonic, I_6, is a specific combination of Y_{6m} spherical harmonics that remains invariant under all rotations that are symmetries of an icosahedron. After that comes I_{10}, etc. A combination such as $c_0 I_0 + c_6 I_6$ with $c_6 << c_0$ represents nearly perfect spherical symmetry with a weak icosahedral symmetry breaking.

The vector spherical harmonics $\mathbf{V}_{lm}$, $\mathbf{W}_{lm}$ and $\mathbf{X}_{lm}$ (1) are only one of many choices for the vector field basis set. In our analysis we also use the alternate set in Eq. 9. Given the scalar function $\phi(\mathbf{r}) = F(r) Y_{lm}(\theta, \phi)$, its gradient and angular momentum can be expressed as linear combinations of the vector spherical harmonics through

$$
\begin{aligned}
\nabla \phi(\boldsymbol{r}) &= \left(\frac{l}{r} F - \frac{dF}{dr} \right) \left(\frac{l+1}{2l+1} \right)^{1/2} \mathbf{V}_{lm} \\
&\quad + \left(\frac{l+1}{r} F + \frac{dF}{dr} \right) \left(\frac{l}{2l+1} \right)^{1/2} \mathbf{W}_{lm} \\
\mathbf{L} \phi(\boldsymbol{r}) &= i \left(l(l+1) \right)^{1/2} F \mathbf{X}_{lm} \\
\nabla \times (\mathbf{L} \phi(\boldsymbol{r})) &= l \left(\frac{l}{r} F - \frac{dF}{dr} \right) \left(\frac{l+1}{2l+1} \right)^{1/2} \mathbf{V}_{lm} \\
&\quad -(l+1) \left(\frac{l+1}{r} F + \frac{dF}{dr} \right) \left(\frac{l}{2l+1} \right)^{1/2} \mathbf{W}_{lm}
\end{aligned} \tag{A-6}
$$

Notice that the vector spherical harmonics of type $\mathbf{X}_l$ are always tangent to the sphere. We refer to these modes as "torsional". In contrast vector spherical harmonics of types $\mathbf{V}_l$ and $\mathbf{W}_l$ contain both tangent and radial components, and usually enter solutions of the wave equation in combination with each other. We refer to these modes as "spheroidal".

APPENDIX B: Boundary conditions

Spherical symmetry assures that oscillation frequencies depend on the angular momentum index l but are independent of the azimuthal quantum number m. Since m ranges between $-l$ and $+l$, a mode of angular momentum index l has degeneracy $2l + 1$. The value $m = 0$ yields modes of specially simple form because $\mathbf{u}_0$ becomes independent of the azimuthal angle ϕ. Specifically,

$$
\begin{aligned}
\mathbf{u}_0(r) = c_0 & \left(qj'(qr)Y_l(\theta)\hat{\mathbf{r}} + \frac{j(qr)}{r}\frac{\partial Y_l(\theta)}{\partial\theta}\hat{\boldsymbol{\theta}} \right) \\
+ c_1 & \left(j(kr)\frac{\partial Y_l(\theta)}{\partial\theta}\hat{\boldsymbol{\phi}} \right) \\
+ c_2 & \left(-l(l+1)\frac{j(kr)}{r}Y_l(\theta)\hat{\mathbf{r}} - \left[\frac{j(kr)}{r} + kj'(kr) \right]\frac{\partial Y_l(\theta)}{\partial\theta}\hat{\boldsymbol{\theta}} \right),
\end{aligned}
\tag{B-1}
$$

where the functions $Y_l(\theta) \equiv Y_{l0}(\theta,\phi)$ do not depend on ϕ, and c_0, c_1 and c_2 are as-yet undetermined constants. The coefficient c_1 multiplies the $\hat{\boldsymbol{\phi}}$ terms, tangent to the surface of the sphere, corresponding to *torsional* modes. The other two coefficients, c_0 and c_2 multiply the $\hat{\mathbf{r}}$ and $\hat{\boldsymbol{\theta}}$ terms, and correspond to *spheroidal* modes.

Substituting the above general solution into the boundary condition Eq. 14, we obtain

$$
\begin{bmatrix} A_{11} & 0 & A_{13} \\ 0 & A_{22} & 0 \\ A_{31} & 0 & A_{33} \end{bmatrix} \begin{bmatrix} c_0 \\ c_1 \\ c_2 \end{bmatrix}\Bigg|_{r=R} = 0
\tag{B-2}
$$

3

where

$$A_{11} = (1 - \sigma)q^2 j''(qr) + 2\sigma \frac{qj'(qr)}{r} - \sigma l(l+1)\frac{j(qr)}{r^2}$$

$$A_{13} = (2\sigma - 1)l(l+1)\left(\frac{kj'(kr)}{r} - \frac{j(kr)}{r^2}\right)$$

$$A_{22} = kj'(kr) - \frac{j(kr)}{r} \tag{B-3}$$

$$A_{31} = 2\left(\frac{qj'(qr)}{r} - \frac{j(qr)}{r^2}\right)$$

$$A_{33} = (2 - l(l+1))\frac{j(kr)}{r^2} - k^2 j''(kr)$$

Notice that in Eq. B-2 the coefficient matrix separates into two sub-matrices. One submatrix multiplies the coefficient c_1, the other multiplies c_0 and c_2. Nonzero solutions to Eq. B-2 exist only if the determinant of the matrix vanishes. Since the matrix divides into two sub-matrices, the solvability condition becomes

$$A_{22}|_{r=R} = 0 \tag{B-4}$$

and

$$\det \begin{vmatrix} A_{11} & A_{13} \\ A_{31} & A_{33} \end{vmatrix}\bigg|_{r=R} = 0 \tag{B-5}$$

By solving the above equations, for each angular momentum index l, the transverse wavenumber k can be extracted, yielding the vibrational frequency $\omega = c_t k$ and the "eigenvalue" $\lambda^{(cont)} = \omega^2$.

APPENDIX C: Mackay icosahedron and toy models

This appendix contains tables and figures relating to our toy models based on the Mackay icosahedron. See main text for discussion.

Mode #	Eigenvalue (ps^{-2})	Icosahedral Representations	Vector Spherical Representations
1-5	1.36451	H	$\mathbf{X}_2$
6-10	1.64639	H	$\mathbf{V}_2 + \mathbf{W}_2$
11-13	2.64211	F_1	$\mathbf{V}_1$
14-17	3.09554	G	$\mathbf{X}_3$
18-20	3.26970	F_2	
21-23	3.42060	F_2	$\mathbf{V}_3 + \mathbf{W}_3$
24-27	3.63187	G	
28	4.55380	A	$\mathbf{V}_0$

Table C-1: ANM eigenvalues and mode types of our solid sphere toy model. Icosahedral symmetry breaking $\rho_6/\rho_0 = 0.0026$. Representations are discussed in Appendix A.

Mode #	Eigenvalue (ps^{-2})	Icosahedral Representations	Vector Spherical Representations
1-5	0.89990	H	$\mathbf{V}_2 + \mathbf{W}_2$
6-10	1.30453	H	$\mathbf{X}_2$
11-13	2.24883	F_2	$\mathbf{V}_3 + \mathbf{W}_3$
14-17	2.40630	G	
18-20	2.96895	F_1	$\mathbf{V}_1$
21	2.98536	A	$\mathbf{V}_0$
22-25	3.02320	G	$\mathbf{X}_3$
26-28	3.21800	F_2	

Table C-2: ANM eigenvalues and mode types of our hollow sphere toy models. For the hollow sphere we set the radius ratio $R_2/R_1 = 2$. Icosahedral symmetry breaking $\rho_6/\rho_0 = 0.0376$.
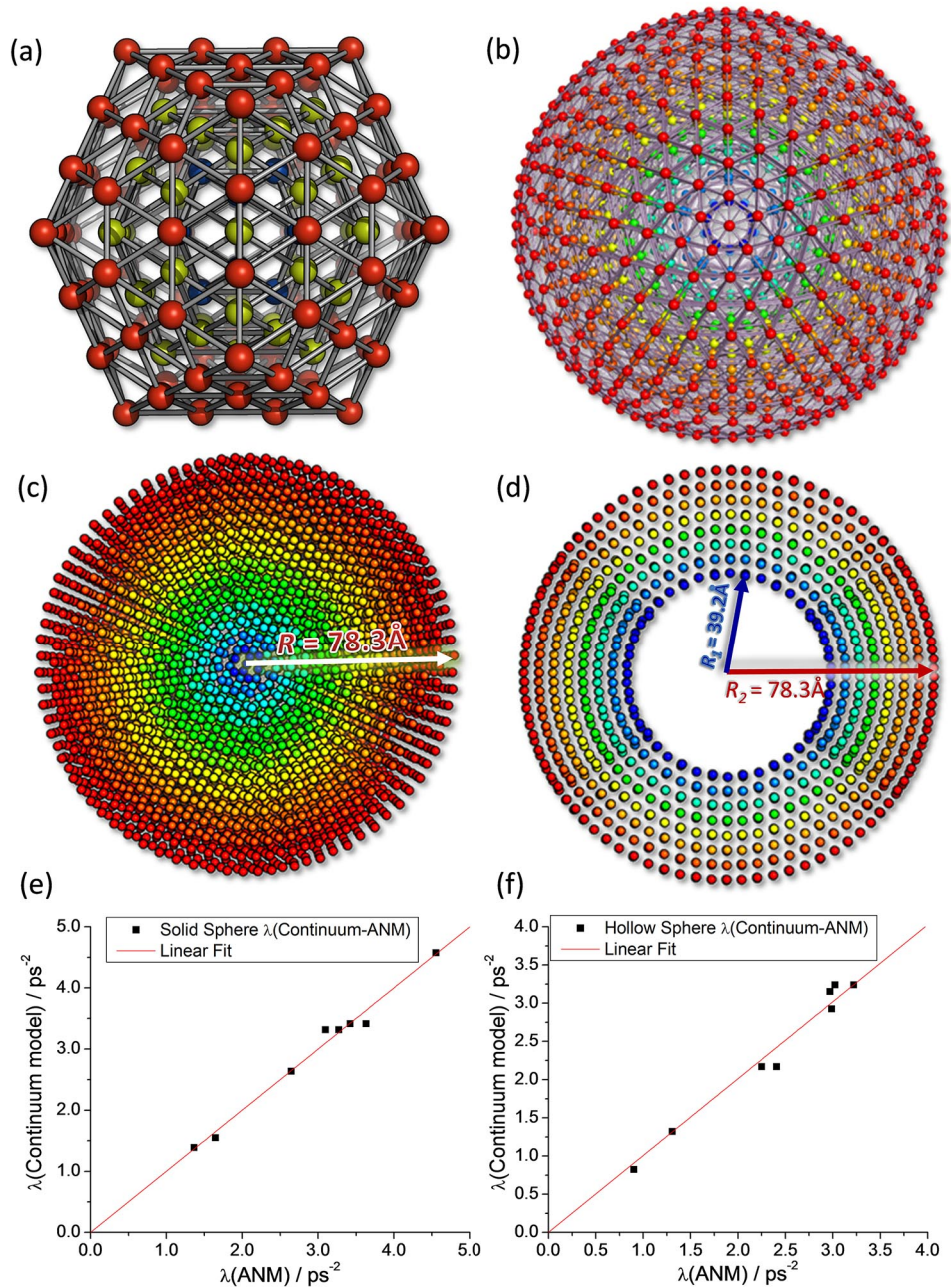
Figure C-1: Mackay icosahedrons and corresponding toy models of spherical symmetry. (a) Three-layer Mackay icosahedrons. (b) Sphere constructed using Mackay icosahedral symmetry for the nodes. (c) Cross-sectional view of the sphere displayed in panel b. (d) Cross-sectional view of a hollow sphere with indicated inner and outer radii. Panels (a-d) are colored by layer radius, from blue (small) to red (large). (e) Comparison of the dispersion of modes (distribution of eigenvalues) predicted by ANM and by the continuum model for the model shown in panel (c). (f) Same as panel (e), for the hollow sphere model in (d).

APPENDIX D: STMV full capsid

In addition of the empty STMV capsid, the same calculation was preformed on STMV partially filled with its genome (4).For each RNA nucleotide, atoms P, C2 and C4' were taken as nodes of the elastic network (see Fig. D-1). The inner radius R_1 drops from 55.4 Å to 44.2 Å. The resulting eigenvalues are listed in Table D-1. Notice that the modes with $l = 1$ appear at lower frequency when RNA is included ($l = 1$ appears in modes 28-30 with RNA; are modes 36-38 without RNA). Likewise, the eigenvalue of the $l = 2$ spheroidal squeezing modes (modes 1-5) increases by 8% in the presence of the
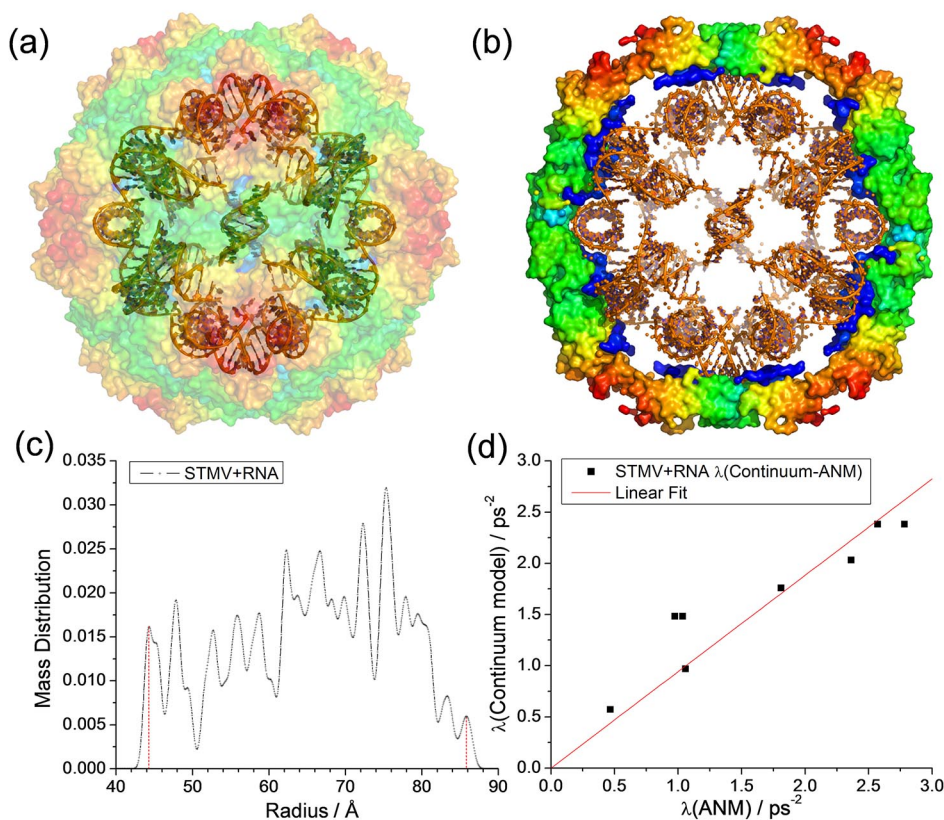

Figure D-1: Results for STMV filled capsid. (a) 3D structure of STMV (PDB file: 1A34 (4), capsid plus genome), with the surface colored by geometric position to illustrate the icosahedral symmetry. (b) Cross-sectional view of the same structure. (c) mass distribution as a function of radial position, used as basis for defining the inner and outer radii of the hollow sphere model used in continuum elasticity theory, and (d) comparison of the ANM eigenvalues with those found by the continuum elasticity theory for a hollow sphere with the same dimensions and packing density.

genome, while the $l = 2$ torsional twisting modes (modes 13-17) increase by only 0.4%.

Mode #	Eigenvalue (ps^{-2})	Icosahedral Representations	Vector Spherical Representations
1-5	0.46662	H	$\mathbf{V}_2 + \mathbf{W}_2$
6-8	0.97430	F_2	$\mathbf{V}_3 + \mathbf{W}_3$
9-12	1.03662	G	
13-17	1.05818	H	$\mathbf{X}_2$
18-21	1.61848	G	$\mathbf{V}_4 + \mathbf{W}_4 + \mathbf{X}_3$
22	1.81089	A	$\mathbf{V}_0$
23-27	2.12701	H	$\mathbf{V}_4 + \mathbf{W}_4 + \mathbf{V}_2$
28-30	2.36294	F_1	$\mathbf{V}_1$

Table D-1: ANM eigenvalues and mode types of STMV (capsid+RNA). Icosahedral symmetry breaking $\rho_6/\rho_0 = 0.0166$

APPENDIX E: Brome Mosaic Virus

$T = 1$ particle of brome mosaic virus (ID:1YC6, abbreviated as BMV) is assembled *in vitro* from the wild-type $T = 3$ brome mosaic virus under certain chemical conditions (5). Unlike STMV, it has a strong reduction of spherical symmetry to icosahedral ($\rho_6/\rho_0 = 0.1029$, see Appendix A) and is proves useful to contrast the spherical continuum model with this extreme case.

The inner and outer radii are $R_1 = 54.5$ Å and $R_2 = 95.0$ Å respectively. Despite the strong deviation from spherical symmetry, we obtain a tolerable fit of continuum elastic eigenvalues to our ANM model. We find $E/\gamma = 6.58 \pm 0.2$ nm^{-1} and $\sigma = 0.30$ with MSD of 0.0016 ps^{-4}. The lower magnitude of the Young's modulus for BMV compared with the other examined models is because the irregular structure of BMV (Fig. E-1) leads to an overall lower packing density.

Although we still identify a dominant vector spherical harmonic, as given in Table E-1, we now find significant contributions from other vector spherical harmonics, as given in parenthesis following the dominant contribution. These secondary contributions were identified on the basis of the projection method outlined in Appendix A. The secondary contributions follow patterns that can be explained on the basis of icosahedral symmetry together with addition of angular momentum laws that we present below. Although the ANM eigenvectors no longer correspond cleanly to vector spherical harmonics, we can still
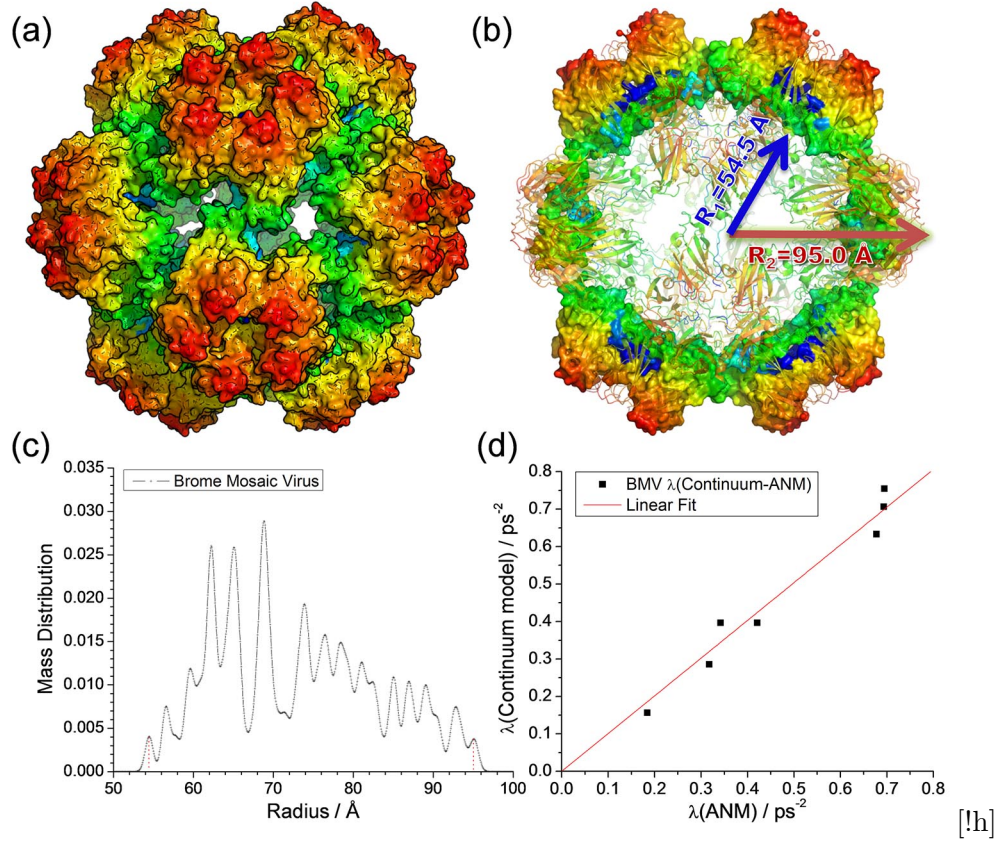
Figure E-1: (a) 3D structure of BMV (PDB file: 1YC6 (5)), with the surface colored by geometric position to illustrate the icosahedral symmetry. (b) Cross-sectional view of the same structure. (c) mass distribution as a function of radial position, used as basis for defining the inner and outer radii of the hollow sphere model used in continuum elasticity theory, and (d) comparison of the ANM eigenvalues with those found by the continuum elasticity theory for a hollow sphere with the same dimensions and packing density.

label them uniquely according to icosahedral irreducible representations.

For weakly icosahedral structures such as LS and STMV, each mode could be identified with a specific vector spherical harmonic type. In contrast, for the strongly icosahedral BMV structure we found admixtures of extra vector spherical harmonic types in each mode. This behavior is an expected result of icosahedral perturbations on an otherwise spherical structure. Specifically, each mode belongs to a unique icosahedral irreducible representation, but many different vector spherical harmonics may transform under the same icosahedral representation (e.g. according to Table 1 the nondegenerate mode of

9

icosahedral type A belongs to angular momentum $l = 0$ and $l = 6$ but no angular momenta in between). The results for BMV obey these relationships (e.g. according to Table E-1, mode #18 of type A projects only onto $l = 0$ and $l = 6$).

The symmetry classification governs what combinations of modes are permissible, but does not guarantee they will all occur in practice. To understand what mixtures will actually occur requires a mechanism to couple the different vector spherical harmonics. Addition of angular momentum laws (6) provide one such mechanism. Start with the equation of motion, Eq. 3 in the form

$$\ddot{\mathbf{u}} = \frac{\mu}{\rho}\nabla^2\mathbf{u} + \frac{\lambda + \mu}{\rho}\nabla\nabla \cdot \mathbf{u} \tag{E-1}$$

and consider slow spatial variation of the material parameters μ/ρ and λ/ρ. These variations respect icosahedral symmetry and the parameters can therefore be expanded in a series of icosahedral harmonics (see Appendix A) as $c_0 I_0 + c_6 I_6$. When we substitute a vector spherical harmonic of angular momentum l for the variable $\mathbf{u}$ in the wave equation (Eq. E-1) it gets multiplied by a term of angular momentum $l' = 0$ and a relatively weak term of angular momentum $l' = 6$. According to laws of angular momentum addition (6), multiplication of l by $l' = 0$ does not alter the value of l. However, multiplication of l by $l' = 6$ will produce a series of additional angular momenta l'', ranging from $6 - l$ up to $6 + l$.

In such a manner, modes of icosahedral type H and angular momentum $l = 2$ necessarily contain admixtures of momentum $l = 4$, and the nondegenerate mode of icosahedral type A and angular momentum $l = 0$ mixes with an icosahedrally symmetric combination of

Mode #	Eigenvalue (ps^{-2})	Icosahedral Representations	Vector Spherical Representations
1-5	0.18428	H	$\mathbf{W}_2 + \mathbf{V}_2$ $(\mathbf{X}_2 + \mathbf{X}_4 + \mathbf{V}_4)$
6-10	0.31746	H	$\mathbf{X}_2$ $(\mathbf{X}_4 + \mathbf{W}_2 + \mathbf{V}_4)$
11-14	0.34180	G	$\mathbf{V}_3 + \mathbf{W}_3$ $(\mathbf{X}_3)$
15-17	0.42087	F_2	$\mathbf{V}_3 + \mathbf{W}_3$ $(\mathbf{X}_3)$
18	0.67744	A	$\mathbf{V}_0$ $(\mathbf{W}_6 + \mathbf{X}_6)$
19-22	0.69309	G	$\mathbf{X}_3$ $(\mathbf{V}_4 + \mathbf{V}_3 + \mathbf{W}_3)$
23-25	0.69450	F_1	$\mathbf{V}_1$ $(\mathbf{X}_5 + \mathbf{W}_5 + \mathbf{V}_5)$

Table E-1: ANM eigenvalues and mode types of BMV. Icosahedral symmetry breaking $\rho_6/\rho_0 = 0.1029$. Vector spherical representations in parenthesis are secondary contributions.

angular momentum $l = 6$. Angular momentum $l = 3$ largely remains intact. These patterns are visible in Table E-1.

The mechanism just discussed preserves the torsional and spheroidal nature of the modes. Therefore modes should remain purely of type $\mathbf{X}$ or $\mathbf{V} + \mathbf{W}$. Inspecting Table E-1 we see this is not the case, for example $\mathbf{X}_2$ mixes with $\mathbf{V}_2 + \mathbf{W}_2$. A likely explanation for mixing of torsional and spheroidal mode types lies in the boundary conditions. The boundary condition couples torsional and spheroidal modes whenever the surface normal $\hat{\boldsymbol{n}}$ is not in the radial direction $\hat{\boldsymbol{r}}$. Furthermore, as a vector $\hat{\boldsymbol{r}}$ carries angular momentum $l' = 1$. Hence the $\mathbf{X}_3$ mode can mix with mode $\mathbf{V}_4$, etc.

References

1. Hill, E. L., 1954. The theory of vector spherical harmonics. *Am. J. Phys.* 22:211–214.

2. Steinhardt, P. J., D. R. Nelson, and M. Ronchetti, 1983. Bond-orientaional order in liquids and glasses. *Phys. Rev. B.* 784–805.

3. Yin, Z., Y. Zheng, and P. C. Doerschuk, 2001. An *ab initio* algorithm for low-resolution 3-D reconstructions from cryoelectron microscopy images. *J. Struct. Biol.* 133:132–42.

4. Larson, S. B., J. Day, A. Greenwood, and A. McPherson, 1998. Refined structure of satellite tobacco mosaic virus at 1.8 Å resolution. *J. Mol. Biol.* 277:37–59.

5. Larson, S. B., R. W. Lucas, and A. McPherson, 2005. Crystallographic structure of the T=1 particle of brome mosaic virus. *J. Mol. Biol.* 346:815–831.

6. Tinkham, M., 1964. Group theory and quantum mechanics. McGraw Hill.